Non-reflecting boundaries for ultrasound in fluctuating hydrodynamics of open systems.

R. Delgado-Buscalioni[1,*] and A. Dejoan[2,†]

[1] *Depto. Física Teorica de la Materia Condensada, Universidad Autónoma de Madrid, Campus de Cantoblanco, Madrid, E-28049, Spain.*

[2] *Depto. Energía, Unidad de Simulación Numérica y Modelización de Procesos, CIEMAT, Avenida Complutense 22 Edificio 20, 28040-Madrid, Spain*

(Dated: July 21, 2008)

We present a formulation for non-reflecting boundaries in fluctuating hydrodynamics. Non-reflecting boundary conditions (NRBC) are designed to evacuate sound waves out of the computational domain, thus allowing to deal with open systems and to avoid finite size effects associated with periodic boundaries . Thermodynamic consistency for the fluctuation of the total mass and momentum of the open system is ensured by a fluctuation-dissipation balance which controls the amplitude of the sound waves generated by stress fluctuations near the boundary. We consider equilibrium and out-of-equilibrium situations (forced sound) in liquid water at ambient conditions and argon ranging from gas to liquid densities. Non-reflecting boundaries for fluctuating hydrodynamics makes feasible simulations of ultrasound in microfluidic devices.

I. INTRODUCTION

During the last decade the interest in microfluidics has grown dramatically due to applications in industry. At these small scales, fluid flow can be described by *fluctuating hydrodynamics* [1] characterized by stress and heat flux fluctuations arising from the chaotic series molecular collisions underlying the coarse-grained hydrodynamic level [2]. Fluctuating hydrodynamics (FH) deals with small lumps of fluids (from micrometers to nanometers) so the generalization of the *non-reflecting boundary condition* (NRBC) presented here is meant to become a useful tool in simulations involving sound in nano and microfluidics. At such small wavelengths, sound waves oscillate at frequencies of the order of MHz-GHz, corresponding to the ultrasound regime. Ultrasound is used in a large list of technological and medical applications, which is still being explored. An interesting example is the possibility of producing devices to collimate sound [4], whose computational study clearly requires NRBC. Another broad field of fundamental and technological interest is ultrasound-particle interaction, which is being used to characterize colloidal suspensions or to transport and manipulate nanoparticles [5]. Ultrasound-particle simulations are however scarce in the literature and have been limited to standing waves solved using periodic boundary conditions (PBC) via the lattice Boltzmann method, see e.g. Ref. [6].

In fact, fluctuating hydrodynamics has been so far applied using either rigid walls (RW) or periodic boundary conditions (PBC), whereby the system folds to itself and no conditions are required at the boundaries. However, these kind of boundary conditions considerably limits the range of applications. When dealing with real devices one usually needs to consider general boundaries which enable to "open up" one or several boundaries of the simulation domain. Open boundary conditions are usually required when one is interested in resolving the flow within a part of the total system (a window); an archetypal example being the flow within a channel having a non equilibrium pressure (or density) profile. In the same way, simulations involving traveling waves require non-reflecting boundaries which enable to evacuate sound out of the system. More generally, open boundaries can be used to let vortices or heat travel outside the simulation window. While there has been considerable theoretical and numerical work on open boundary conditions in standard computational fluid dynamics (CFD) [3], to the best of our knowledge there has been no attempt to apply these ideas to fluctuating hydrodynamics. A key issue in fluctuating hydrodynamics is to take into account the exchange of mass, momentum and energy between the open system and its surroundings. Such exchange needs to be expressed in the form of a fluctuation-dissipation balance, ensuring that the variance of mass, momentum and energy of the total (open) system satisfies the thermodynamic prescriptions.

In a more general context, flow-particle interactions are receiving a great deal of attention in several fields (and scales) ranging from an ensemble of particles in open turbulent flow to one single complex molecule in low Reynolds number flow. Consequently, computational methods designed to couple fluid and particle motion have been developed

*rafael.delgado@uam.es

†anne.dejoan@ciemat.es

for different scenarios (such as turbulence, lattice Boltzmann [7] or fluctuating hydrodynamics codes [8]). The NRBC formulation allows to extend the range of applications of these computational approaches. The present generalization of the method can be straightforwardly implemented in fluctuating lattice Boltzmann codes [9] and it might be useful for simulations of compressible turbulent flow in open system. Non-reflecting boundaries for fluctuating hydrodynamics (FH) will also prove to be useful in hybrid particle-continuum schemes based on domain decomposition and flux exchange [10, 11]. Hybrid codes, coupling either Direct Simulation Monte Carlo (DSMC) and FH [11] or molecular dynamics (MD) and FH [10, 13], enable to study the fluid-particle interaction directly from the underlying solvent-solute molecular collisions, i.e. without assuming any phenomenological coupling law (such like the Stokes force). Flux based hybrid methods can solve unsteady flow and have been applied to study the interaction between flow and complex molecules (such as polymers in flow [14, 15] or sound waves against molecular assemblies [16]). In this context, the NRBC provides a natural way to evacuate sound waves out of the particle domain, through the open borders of the embedding hydrodynamic region.

In what follows we first present the fluctuating hydrodynamics equations then, in Sec. III, we present the NRBC formalism. In Sec. IV we show that the only free parameter of the NRBC formulation can be evaluated from a fluctuation-dissipation balance which fits the variance of the total mass of the open system to its proper thermodynamic value. Section V presents results for the equilibrium state and non-equilibrium (forced waves) situations. Finally, conclusions are given in Sec. VI.

II. FLUCTUATING HYDRODYNAMICS EQUATIONS

We shall focus on the treatment of open boundary conditions for sound waves in fluctuating hydrodynamics. Fluctuating hydrodynamics deals with flow within micron and submicron scales, and we shall consider sound waves with wavelengths of about $\lambda \in [10 - 1000]$ nm, corresponding to frequencies in the MHz-GHz (ultrasound) regime. Due to its broad range of applications we consider water at ambient pressure and T =300 K. The adiabatic constant (i.e. the specific heat ratio, $\gamma = c_P/c_V$) of liquid water is almost unity, ($\gamma = 1.0106$) so one can neglect the effect of temperature variations in the sound induced pressure fluctuations. We thus assume $\gamma = 1$, which corresponds to a fluid with equal isothermal and adiabatic sound velocities. Sound propagates adiabatically and as in any adiabatic process, temperature and density flucutations are related as $(\partial p/\partial T)_\rho \delta T = (\gamma - 1)(\partial p/\partial \rho)_T \delta\rho$. Thus for $\gamma = 1$, momentum and temperature equations are decoupled and sound is uniquely governed by mass and momentum equations.

We shall therefore consider the mass continuity and momentum equations for fluctuating hydrodynamics of a fluid with velocity components u_i ($i = \{x, y, z\}$), density ρ and fixed temperature, T:

$$\frac{\partial \rho}{\partial t} + \frac{\partial \rho u_i}{\partial x_i} = 0 \tag{1}$$

$$\frac{\partial \rho u_i}{\partial t} + u_j \frac{\partial \rho u_i}{\partial u_j} = -\frac{\partial}{\partial x_j}\left(p\delta_{ij} + \Pi_{ij}\right), \tag{2}$$

where the right hand side of equation (2) represents the full pressure tensor: p is the thermodynamic pressure and Π_{ij} is the stress tensor, which can be decomposed into a mean contribution $\overline{\Pi}_{ij}$ and a fluctuating part $\widetilde{\Pi}_{ij}$. The mean viscous tensor is given by

$$\overline{\Pi}_{ij} = -\left[\eta\left(\frac{\partial u_i}{\partial x_j} + \frac{\partial u_j}{\partial x_i} - \frac{2}{3}\frac{\partial u_l}{\partial x_l}\delta_{ij}\right) + \xi\frac{\partial u_l}{\partial x_l}\delta_{ij}\right], \tag{3}$$

where η and ξ are respectively the longitudinal and bulk viscosities and summation is indicated over repeated subindexes.

The fluctuating tensor is written according to Serrano and Español *et al.*[12],

$$\widetilde{\Pi}_{ij} = A\left[\frac{dW_{ij} + dW_{ji}}{2} - \frac{dW_{ll}}{3}\right] + B\frac{dW_{ll}}{3}, \tag{4}$$

where dW_{ij} is a random matrix of unit variance and the coefficients A and B are given by

$$A = \left(4k_bT\frac{\eta}{V_c}\right)^{1/2}, \tag{5}$$

$$B = \left(2Dk_bT\frac{\xi}{V_c}\right)^{1/2}. \tag{6}$$

where k_b is the Boltzmann's constant, V_c the cell volume and the spatial dimension is $D = 3$.

The covariance of the random stress is given by,

$$< \widetilde{\Pi}_{ij}(x,t)\widetilde{\Pi}_{kl}(x',t') >= \frac{2k_bT}{V_c}\left[\eta\left(\delta_{ik}\delta_{jl} + \delta_{ij}\delta_{kl} - \frac{2}{3}\delta_{ij}\delta_{kl}\right) + \xi\delta_{ij}\delta_{kl}\right]\delta(x-x')\delta(t-t'), \tag{7}$$

so that the correlation of the longitudinal components are,

$$< \widetilde{\Pi}_{xx}(x,t)\widetilde{\Pi}_{xx}(x',t') >= \frac{2k_bT}{V_c}\left(\frac{4}{3}\eta + \xi\right)\delta(x-x')\delta(t-t'). \tag{8}$$

The equations of continuity and momentum are completed by the equations of state $p = p(\rho, T)$ and the constitutive relations for the shear and bulk viscosity $\eta = \eta(\rho, T)$ and $\zeta(\rho, T)$, respectively. As stated we considered water at $T = 300$K and ambient pressure. The equation of state $p = p(\rho)$ and viscosities corresponds to the TIP3P water model at $T = 100$K used in MD and obtained in a previous work [17] (see Fig. 1). In order to test the model against a broader range of thermodynamic and fluid conditions we also considered argon at several densities and temperatures (see Refs. [18] and Fig. 1 for the equation of state and [19] for viscosities). The adiabatic constant of argon is larger than one ($\gamma \simeq 1.5$) so in assuming $\gamma = 1$ we underestimate the sound velocity of argon. However, in doing so, neither the physics of sound nor the open boundary model are essentially altered (see Sec. III C).

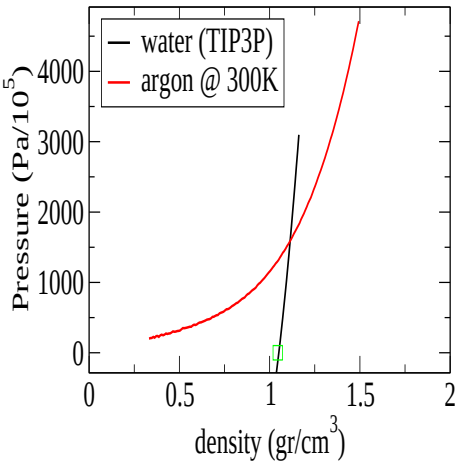

FIG. 1: Pressure equation of state at $T = 300$K for argon (Lennard-Jones model) and water (TIP3P model).

III. NON-REFLECTING OUTFLOW BOUNDARY CONDITIONS

Open boundary conditions are needed in most practical cases involving fluid dynamics processes. To that end Poinsot & Lele [20] derived the Navier-Stokes Characteristic Boundary Conditions (NSCBC) procedure for deriving different kinds of boundary conditions in computational fluid dynamics from physical grounds. The central idea is to use relations based on the analysis of the different waves crossing the boundaries of the computational domain. The NSCBC method is an extension of the Euler Characteristic Boundary Condition methodology used for specifying boundary conditions in hyperbolic systems (Euler equations) [21], [22]. Our main purpose here is to apply the NSCBC approach to outflow boundary conditions of open fluctuating hydrodynamics systems.

A. General formulation

Linear dynamics of a monocomponent fluid can be expressed in terms of five *normal modes*, also called *characteristic waves*: two sound waves (traveling in opposite directions), one heat wave and two shear waves in perpendicular directions [23]. There is no exact method to specify the values of the characteristic waves amplitudes for multi-dimensional Navier-Stokes equations in an arbitrary geometry. However, this can be done for the one-dimensional

inviscid equations. The NSCBC approach is to infer values for the wave amplitude variations in the general 3D viscous case by extracting the local characteristic waves traveling across the *normal-to-boundary* direction from the so called *local one-dimensional inviscid* (LODI) problem [3], [24]. Consider a flow near a boundary whose normal direction is x. The flow velocity near the boundary is u_{BC}, and the fluid sound velocity c. The amplitude of the characteristic sound waves A_i arising from the linearized inviscid problem in x direction, is conserved along the characteristic line $x \pm \lambda_i t = cste$ (where λ_i is the characteristic wave velocity, see Eq.12) so that $\partial A_i/\partial t + \lambda_i \partial A_i/\partial x = 0$. According to the notation used in Ref. [24], $i = 1$ corresponds to the left-wise ($\leftarrow$) moving sound wave, $i = 5$ to the right-wise ($\rightarrow$) sound wave, $i = 2$ to the entropy advection mode ($A_2 = s$) and $i = 3, 4$ to the two perpendicular shear modes (e.g, $A_3 = v$ is one velocity normal to x direction).

The acoustic mode amplitudes are given by

$$A_1 = \frac{1}{2}\left(\frac{\delta p}{\rho_e c} - \delta u\right) \quad \text{wave moving} \leftarrow \tag{9}$$

$$A_5 = \frac{1}{2}\left(\frac{\delta p}{\rho_e c} + \delta u\right) \quad \text{wave moving} \rightarrow \tag{10}$$

A_1 and A_5 are also called the Riemann invariants associated with the acoustic waves propagating in left-wise (A_1) and right-wise x-direction (A_5). The amplitudes A_1 and A_5 are defined in terms of perturbations of flow variables with respect to the corresponding equilibrium value: $\delta p = p - p_e$ and $\delta u = u - u_e$.

By noting that $A_1 + A_5 = \delta p/(\rho_e c)$ and $A_1 - A_5 = \delta u$ and by introducing in the momentum equation (2) the followig quantities L_1 and L_5

$$\begin{aligned} L_1 &= \lambda_1 \left(\frac{\partial p}{\partial x} - \rho_e c \frac{\partial u}{\partial x}\right) \\ L_5 &= \lambda_5 \left(\frac{\partial p}{\partial x} + \rho_e c \frac{\partial u}{\partial x}\right) \end{aligned} \tag{11}$$

where λ_i are the characteristic velocities

$$\begin{aligned} \lambda_1 &= u - c \\ \lambda_5 &= u + c \end{aligned} \tag{12}$$

one can write the LODI relations used to determine the boundary conditions for the pressure and velocity [22]

$$\frac{\partial p}{\partial t} + \frac{1}{2}\left(L_5 + L_1\right) = 0 \tag{13}$$

$$\frac{\partial u}{\partial t} + \frac{1}{2\rho_e c}(L_5 - L_1) = -\frac{1}{\rho_e}\frac{\partial}{\partial x}\left(\Pi_{xx}\right). \tag{14}$$

Physically, the operators L_1 and L_5 represent as the the temporal rate of change of wave amplitudes at the boundary [24] and are thus called the sound wave amplitude variations. Indeed, $L_i = 2\rho_e c \lambda_i \partial A_i/\partial x = -\partial A_i/\partial t$.

Regarding the density, the LODI relation writes as follows

$$\frac{\partial \rho}{\partial t} + \frac{1}{c^2}\left[\frac{1}{2}\left(L_5 + L_1\right) + L_2\right] = 0. \tag{15}$$

where L_2 is related to the entropy advection mode and given by

$$L_2 = \lambda_2 \left(c^2 \frac{\partial \rho}{\partial x} - \frac{\partial p}{\partial x}\right) \quad \text{with} \quad \lambda_2 = u \tag{16}$$

In our case we don't consider heat transport so that $\delta p = c^2 \delta \rho$ which implies $L_2 = 0$. The equation for the density is thus redundant with Eq. (13).

Finally, in the viscid case, the amplitudes of the sound waves travelling left and right-wise are ruled by,

$$\frac{\partial A_i}{\partial t} + \frac{L_i}{2\rho_e c} = \pm \frac{1}{2\rho_e}\frac{\partial \Pi_{xx}}{\partial x}, \tag{17}$$

where the sign + at the left hand side of the equation corresponds to A_1 (sign − to A_5).

The NSCBC approach relies on the determination of the L_i's at (or near) the boundary. In principle, one can use Eq. (11) to calculate L_i from the local gradients of pressure and velocity. However, one needs to distinguish the sense of the wave propagation required for this evaluation. In particular, L_1 is associated to waves propagating left-wise in x direction (while L_5 corresponds to waves moving right-wise). Hence, if for example, we consider the *east* boundary of a 1D domain: A_5 is a wave moving outwards, but within the domain, while A_1 moves inwards, coming from outside. Thus, while L_5 can be estimated using the pressure and velocity at interior points, to guess L_1 one needs some extra information (some condition at the exterior). This guess is one of the essential tricks of the trade. In the foregoing discussion, for the sake of clarity, we shall always consider the *east* boundary so that L_5 is associated to outgoing waves and L_1 to incoming waves, as illustrated in Fig. 2.

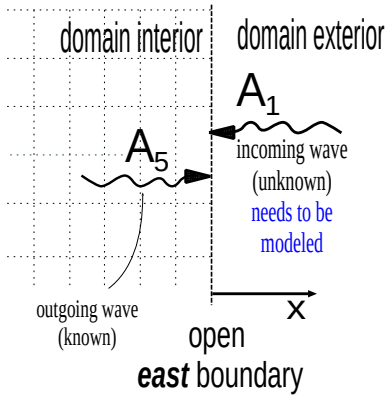

FIG. 2: Incoming and outgoing sound waves through the *east* boundary.

Once the L_i's are known, Eqs. (15)-(14) are then used to compute all other variables required at the boundary. This last step requires boundary conditions for the viscous terms involving normal derivatives to the boundary. According to the theoretical results of Strikwerda [25] and Oliger & Sundstrom [26] one usually imposes weak viscous conditions at the border. In practice this means a vanishing normal stress $\partial\Pi_{xx}/\partial x = 0$, in the right hand side of Eq. (14). This approximation is justified by Poinsot et and Veynante [24]: viscous terms are already explicitly solved inside the domain, so the amplitude L_5 (which is measured *inside*) already contains viscous effects. In agreement with this statement, we tested Eq. (14) with and without the viscous term, and found similar outcomes.

B. Non-reflecting outflow at fixed pressure

The natural choice for building a non-reflecting outlet condition according to the NSCBC approach would be to impose the amplitude variation of the incoming wave L_1 to zero, $L_1 = 0$. However, this condition leads to large drift of the mean pressure. Physically, a perfectly non-reflecting boundary condition can be ill-posed. Indeed, the information on the mean pressure is conveyed by waves reflected into the domain from the outside flow (where the static pressure p_∞ at infinity, or equivalently, the equilibrium pressure p_e is specified). If the local pressure p at the outlet is different from p_e, a reflected wave should be produced to bring p closer to p_e. With perfectly non-reflecting boundary conditions ($L_1 = 0$) this information is not fed back into the computation domain. It is on this physical ground that Rudy & Strikwerda [27] proposed to add information on the mean static pressure at infinity p_e, and write the amplitude of the incoming wave as follows

$$L_1 = K(p - p_\infty) \quad \text{with} \quad K = \frac{\sigma c(1-\mathcal{M}^2)}{L} \tag{18}$$

where L is a characteristic length size of the domain, $\mathcal{M} = u/c$ the Mach number and σ is a constant that has to be fixed. At low Mach number, as those considered in this work, one can write $K = \sigma c/L$.

By inserting Eq. (18) into (13) in absence of outgoing wave ($L_5 = 0$), one sees that the expression (18) can be interpreted as a corrective term that relaxes exponentially the pressure at the frontier to the equilibrium pressure p_e. The relaxation time is $\tau \equiv 1/K = 2L/\sigma c$. Some caution is necessary to estimate the value of the constant σ (see next section): too low values of σ can produce large pressure drift resulting in non-convergence of the calculations, while large values of σ lead to high reflection. Thus, the price one pays for the stability of the scheme is that Eq. (18) yields a partially non-reflecting boundary. This important drawback was recently put forward by Selle *et al.* [28]

and Polifke *et al.* [29]. They proved that although the linear relaxation term (18) leads to an effective non-reflecting boundary for the high-frequency regime (i.e for wave frequencies much larger than the decay rate K), it becomes highly reflecting for the low-frequency range. [34] But in fact these large, low-frequency waves are precisely those one would like to evacuate, because they can travel over long distances before being damped by viscosity. In order to extend the non-reflecting property of the boundary condition to the low-frequency range, Politfke *et al.* [29] proposed the following modification to L_1,

$$L_1 = K(p - \rho c A_5 - p_\infty). \tag{19}$$

This modification applies for plane acoustic waves with normal incidence to the boundary and it is referred as "plane-wave masking". It consists in removing the contribution of the outgoing waves A_5 to the pressure p from the linear relaxation term L_1 so that the (reflected) outgoing wave no longer contributes to the incoming wave A_1. In this way, the incoming wave A_1 is built up to suppress (or to "mask") any reflection contribution from the outgoing wave. The result is that, in practice, A_5 leaves the domain without being reflected. Polifke *et al.* [29] considered acoustic waves in turbulent flow and argue that if deviations from the equilibrium pressure p_e were only caused by plane acoustic waves (i.e. in absence of turbulent fluctuations), the use of Eq. (19) would lead to a vanishing reflection coefficient for plane harmonic waves of arbitrary frequency. However, the results of this work for the (non-turbulent) deterministic regime (i.e., without fluctuations) coincide with those reported in their work [29]. This indicates that the partial reflection observed at short wavelengths ($\lambda/\Delta x < 10$, see Sec. V C) is in fact related to numerical resolution. Also in the fluctuating hydrodynamics context, Eq. (19) stands as the best choice to evacuate most waves ($\lambda/\Delta x > 10$) out of the system.

We now provide more insight into the incoming wave amplitude L_1 proposed in Eq. (19). By using the definition of A_5 in Eq. (10) and the definition of A_1 given by Eq. (9) one gets,

$$L_1 = \frac{K}{2}\left(\delta p - \rho_e c \delta u\right) = K \rho_e c A_1 \tag{20}$$

Using Eq. (17)A_1 is thus governed by

$$\frac{\partial A_1}{\partial t} = -K' A_1 + \frac{1}{2\rho_e}\frac{\partial \Pi_{xx}}{\partial x} \quad \text{with} \quad K' = K/2. \tag{21}$$

Equation (21) sheds more light on how the plane-wave masking controls the incoming waves. In the inviscid limit, the solution of Eq. (21) is simply an exponential decay $A_1 \sim \exp(-K't)$. Hence, the incoming waves are damped at a rate K'. In fact, by damping the incoming wave to its equilibrium value $\langle A_1 \rangle = 0$, one also controls the deviation from the equilibrium pressure, which relaxes to $\langle \delta p \rangle = 0$. By comparison, as stated above, Eq. (18) is only designed to control the overall pressure drift, but not the amplitude of the incoming wave.

It is important to highlight that in the case of fluctuating hydrodynamics, Eq. (21) also acts as a source of incoming random waves. Indeed, the local fluctuating stress near the border is a source of white noise which triggers waves into the system. The boundary condition given in Eq. (21) determines the resulting spectra for the amplitude of incoming waves: at equilibrium the time correlation of incoming waves is a colored noise, $\langle A_1(t) A_1(0) \rangle \propto \exp(-K't)/K'$, and their power spectral density goes like $S_{A_1}(\omega) \propto 1/(\omega^2 + K'^2)$. Implications of this fact are discussed in Sec. IV.

C. Fluctuation-dissipation balance.

In previous works the relaxation time $1/K$ was set proportional to the inverse of sound time over a distance L/σ, i.e. $1/K = L/(\sigma c)$. The constant σ was set according to numerical "optimization" but not based on physical grounds. For instance, when making use of expression (18) for L_1, estimations of the optimal value of σ by Rudy & Strikwerda, provided $\sigma = 0.58$, while Selle *et al.* [28] suggest $0.1 < \sigma < \pi$. By contrasts, by making use of Eq. (19) for L_1, Polifke *et al.* [29] report $\sigma = 167$ as the minimum value required to avoid pressure drift in their computations of a fully developed turbulent channel flow. In this work we address this problem from the perspective of fluctuating hydrodynamics and provide a route to estimate a value of K with physical content. To that end, we consider the fluctuation-dissipation balance for the amplitude of the incoming waves A_1 in the equilibrium state. The overall mass is governed by the amplitude of the incoming waves, so that by imposing the correct variance to A_1 one should get the correct variance for the total mass in the system. In this work the "correct" variance of A_1 comes out from thermodynamic arguments, however we believe that the method proposed here below is more general and it could be applied, for instance, to turbulent flow, provided some knowledge of the amplitude of fluctuations of A_1 (i.e. of pressure and velocity) and of the stress tensor Π.

Let us consider Eq. (21) near the *east* boundary, in particular at the cell face $x_b = x_{f_{n-1}}$ where the NRBC is imposed (see appendix B). We integrate Eq. (21) along a cell volume $V_c = S\Delta x$ around the cell face x_b to get

$$\frac{dA_1(x_b)}{dt} + K' A_1(x_b) = F(t), \tag{22}$$

where we note that in the spirit of the finite volume method $A_1(x_b) = (1/\Delta x)\int_{x_b-\Delta x/2}^{x_b+\Delta x/2} A_1(x)dx$. At equilibrium, the stress has only fluctuating part and its contribution have been collected in the noise term $F(t)$,

$$F(t) \equiv \frac{1}{2\Delta x \rho_e}\left[\Pi_{xx}(x_b + \Delta x/2) - \Pi_{xx}(x_b - \Delta x/2)\right] \tag{23}$$

Equation (22) is a stochastic differential equation which can be solved using standard techniques [30]. The noise source is coming from the local stress tensor, which at equilibrium satisfies [see Eq. (8)],

$$\langle \Pi_{xx}(t)\Pi_{xx}(0)\rangle = \frac{2k_B T \eta_L}{V_c}\delta(t) \tag{24}$$

where $\eta_L = 4\eta/3 + \xi$, is the longitudinal viscosity. Moreover, the fluctuating stress tensor is uncorrelated in space so the time correlation of the noise $F(t)$ satisfies

$$\langle F(t)F(0)\rangle = 2\Phi\delta(t) = \frac{k_B T \eta_L}{\Delta x^2 \rho_e^2 V_c}\delta(t) \tag{25}$$

where the noise amplitude 2Φ is defined from the same equation (25). The fluctuation-dissipation balance, applied to Eq. (22), states that (see e.g [30]),

$$\langle A_1^2\rangle = \frac{\Phi}{K'} \tag{26}$$

At equilibrium the variance of A_1 can be obtained from standard thermodynamics. From Eq. (9) $\langle A_1^2\rangle = (1/4)\left[\langle \delta p^2\rangle/(\rho_e c)^2 + \langle \delta u^2\rangle\right]$. But $\langle \delta p^2\rangle = c^4\langle \delta\rho^2\rangle$, $\langle \delta\rho^2\rangle = \rho_e k_B T/(c^2 V_c)$ and $\langle \delta u^2\rangle = k_B T/(\rho_e V_c)$ so one concludes that,

$$\langle A_1^2\rangle = \frac{1}{2}\frac{k_B T}{\rho_e V_c}. \tag{27}$$

Inserting (27) and (25) into (26) one finally gets the decay rate K' or equivalently of K (see Eq. 21)

$$K' = \frac{\nu_L}{\Delta x^2} \quad \rightarrow \quad K = \frac{2\nu_L}{\Delta x^2} \tag{28}$$

where $\nu_L = \eta_L/\rho_e$ is the kinematic longitudinal viscosity. The result contrasts with the form of K proposed in previous works ($K = \sigma c/L$); in fact Eq. (28) shows no dependence with the sound velocity c or on the system size L. As stated, in this work we consider a fluid with adiabatic constant $\gamma = 1$, such as liquid water. However, we note that the derivation of Eq. (28) remains valid for arbitrary γ [35]. We note that for $\gamma = 1$ the isothermal and adiabatic sound velocities coincide and one can neglect temperature effects on the sound waves while, for compressible fluids such as argon ($\gamma > 1$), one needs to consider the energy equation to consistently solve sound. However, the inclusion of the energy equation in the present open boundary formalism does not require any extra (relaxation) parameter at the boundary. In fact the propagation of the heat mode across the boundary can be solved using the information *within* the computational domain (see Ref. [24]).

In the appendix B we present a numerical implementation of the plane-wave masking boundary conditions for staggered grid which ensures numerical stability for "open" fluctuating hydrodynamics.

IV. MASS FLUCTUATION AT EQUILIBRIUM

As stated above, by ensuring the fluctuation-dissipation balance for the amplitude of the incoming waves one expects to provide the correct variance of total mass, whose value at equilibrium is prescribed by thermodynamics. In

particular, at equilibrium, the mass $M(t)$ of an open system of volume V at temperature T, fluctuates with a variance given by $k_B TV/c^2$, while the variance of the mean density $\bar{\rho}(t) = M(t)/V$ is,

$$\langle(\delta\bar{\rho})^2\rangle = \frac{k_B T}{c^2 V}, \tag{29}$$

where $\delta\bar{\rho} = \bar{\rho} - \rho_e$ is the deviation from the (spatial) mean density with respect to its equilibrium value. The relaxation time $1/K$ for incoming waves should be set so as to guarantee condition (29). According to the fluctuation-dissipation balance set in Eq. (28), the relaxation parameter K should be casted in this form,

$$K = \frac{\nu_L}{(\delta_R \Delta x)^2}. \tag{30}$$

By reference to Eq.(28), the non-dimensional parameter δ_R introduced in Eq. (30) should be $\delta_R = 1./\sqrt{(2)} \sim 0.7$. For the numerical calibration of the open boundary it is important to analyze how the mass variance depends on δ_R. Figure 3 shows the variance of the mean density $\langle(\delta\bar{\rho})^2\rangle$ against δ_R for argon at $\langle\bar{\rho}\rangle = 1.35\text{gm/cm}^3$ (which corresponds to an equilibrium density of $\langle\bar{\rho}\rangle = 0.8\sigma^{-3}$ in Lennard-Jones units) and temperature $T = 300\text{K}$. The mesh size is $\Delta x = 1.377$ nm and the total volume $V = 3371\text{mn}^3$. The total mass fluctuation increases with δ_R (i.e. with the relaxation time $1/K$). According to Fig. 3, for $\delta_R = 0.4$ the mean density variance coincides with the thermodynamic prescription. This value of δ_R shall be called its *optimum* value. The optimum value of δ_R obtained from numerical simulation ($\delta_R = 0.4$) differs slightly from the theoretical prediction in Eq. (28) ($\delta_R = 0.7$). This difference may come out from the way one implements the non-reflecting boundary conditions into the discretized fluctuating hydrodynamics equations (see appendix B) [36]

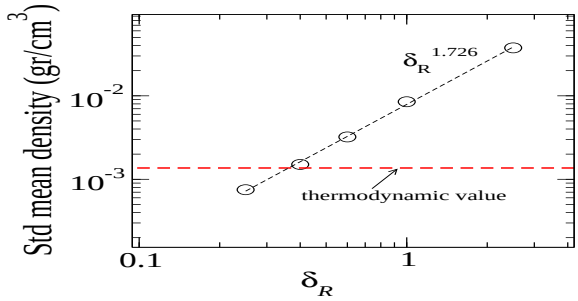

FIG. 3: The standard deviation of the total mass in the simulation domain at equilibrium, versus the parameter δ_R which determines the relaxation rate $K = \nu_L/(\delta_R \Delta x)^2$. Dashed line is the thermodynamic prescription. At the optimum value $\delta_R \simeq 0.4$, the variance of the overall mass coincides with the thermodynamic value.

We tested the theoretical prediction given by Eq. (28) against a broad range of conditions (varying the mesh size Δx, thermodynamic state and fluid properties, using water and argon at several densities). Some results for the standard deviation of the total mass are shown in Table 1. Using $\delta_R = 0.4$ in all cases, the largest differences with respect to the thermodynamic value were about 10%. A finer estimation of the *optimum* δ_R provided $\delta_R = 0.40 \pm 0.04$. We thus conclude that the scheme is robust and that the relaxation parameter K should be set according to Eq. (30), with $\delta_R = 0.4$ [37]. This is also confirmed by the spectral analysis presented below.

In order to understand how the open boundary works, it is instructive to consider the power-spectral density (PSD) of the local density $\rho(x,t)$. The time Fourier-transformed density $\hat{\rho}(x_i,\omega)$ can be used to evaluate the PSD as, $S_\rho(x_i,\omega) = \hat{\rho}(x_i,\omega,)\hat{\rho}^*(x_i,\omega,)$, where * denotes the complex conjugate. We first discuss the behavior of the spatially-averaged PSD, $\bar{S}_\rho(\omega) \equiv (1/N_{cell}) \sum_i S_\rho(x_i,\omega)$, where N_{cell} is the number of cells in the simulation domain. This function is shown in Fig. 4, for a set of values of δ_R. According to fluctuating hydrodynamics, at equilibrium, fluctuations of all possible wavelengths are equally present in the system and one expects to obtain a flat spectra over a wide band of frequencies. We note, however, that all the spectra resulting from the numerical solution of the FH equations shown in Fig. 4 presents a sudden decrease below a cut-off wavelength $\lambda_{cut} \simeq 4\Delta x$. These short waves are in fact filtered out by the numerical resolution, because from a numerical standpoint one cannot describe a sound wave with less than few cells.

Figure 4 illustrates how the parameter δ_R modifies the spectra of sound waves in the system. Large values of δ_R mean small relaxation rates $K = \nu_L/(\delta_R \Delta x)^2$ for which the "source" of incoming waves is slowly relaxed in time. To better understand the effect of the random generation of incoming waves at the border, one can consider the power spectral density (PSD) associated with Eq. (22) given by $S_{A_1} = \Phi/(K^2 + \omega^2)$. At the long-wavelength range (low

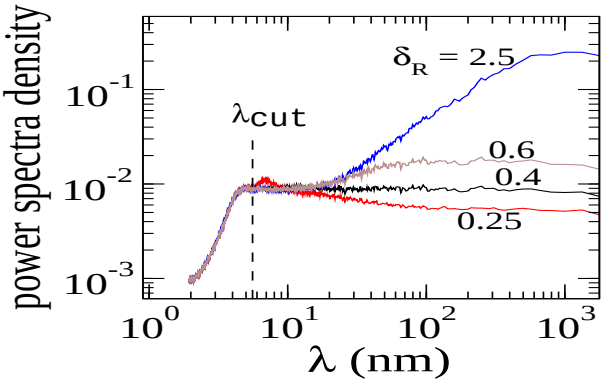

FIG. 4: Spatially averaged PSD of density for liquid argon at $\rho = 1.35$ gr/cm^3 and $T = 300$K versus de wavelenght $\lambda = 2\pi\, c/f$. The cutoff frequency λ_{cut} is indicated at $4\Delta x$. Results corresponds to several values of δ_R, which determines the relaxation rate $K = \nu_L/(\delta_R \Delta x)^2$. The longitudinal viscosity is $\nu_L = 1.9\,10^{-3}$ cm^2/s ($\eta_L = 0.25$ cP). The box size is $L_x = 135nm$ and the grid spacing is $\Delta x = 1.377$nm. The *optimum* δ_R corresponds to $\delta_R = 0.4$.

frequencies, $\omega << K$) the PSD of incoming waves becomes $S_{A_1} \simeq \Phi/K^2 \sim \Phi\delta_R^4$. This means that the amplitude of the long random waves generated at the boundary decreases with the square of the relaxation time $1/K^2$ (i.e. with δ_R^4). This can be clearly seen in Fig. 4 where the presence of longer wavelengths is rapidly increased with δ_R (see the $\delta_R = 2.5$ case). At the short-wavelength range (high frequencies, $\omega >> K$) the PSD of incoming waves becomes K-independent, $S_{A_1} \sim \Phi/\omega^2$. In agreement with this fact, the low-wavelength region of the spectra in Fig. 4 (which takes into account incoming and outgoing wave contributions) does not greatly vary with K or δ_R. We highlight that, precisely at $\delta_R = 0.4$, one gets a flat spectrum over the whole range of allowed frequencies (and even for wavelengths much longer than the system size, see Fig. 5 below).

The mass variance is equal to the integral over the whole frequency range of its power spectral density, thus Fig. 4 clearly indicates that the excess of mass fluctuation observed for large δ_R (see Fig. 3) is due to an excess of long-wavelength waves. In the same way, for low values of δ_R, long waves are over-suppressed and the total mass of the system becomes too much constrained. In conclusion, an optimum value of the relaxation rate K is crucial to control the overall mass variance by providing the correct amount of large-wavelengths into the system.

A. Comparison with periodic boundaries and rigid walls

One of the objectives of this work is to show that open boundary conditions are required in simulations of phenomena involving the propagation of sound waves. Also, when dealing with fluctuating hydrodynamics, and even at equilibrium, the stress fluctuations induce sound waves which might become a significant source of momentum, depending on the boundary condition used. In fluid-particle simulations based on the Stokes friction coupling [8], such momentum is transfered to the solute particles, thus generating spurious forces and non-physical time correlations at sound times. To illustrate this statement, it is quite instructive to compare the sound power spectral densities (at equilibrium) obtained using non-reflecting boundary conditions (NRBC), periodic boundary conditions (PBC) and rigid walls (RW). Such comparison is illustrated in Fig. 5 for a one-dimensional computational domain of dimension $L_x = 135$nm and discretized into 98 cells. For PBC and RW, significant peaks are observed at the natural frequencies of the box [$f_n = n\,c/L_x$ and $f_n = n\,c/(2L_x)$, respectively]. These peaks become quite large as one approaches the fundamental frequency ($n = 1$), corresponding to wavelengths $\lambda = L_x$ in PBC and $\lambda = 2L_x$ in the RW case (in Fig. 5 we indicate the system size wavelength $\lambda = L_x$ with a vertical dashed line). The PSD of the velocity exhibits peaks at identical frequencies. As long as the fluid velocity is used for the Stokes force in fluid-particle simulations, these peaks can induce spurious forces to the particles. As shown in Fig. 5, the NRBC formulation avoids finite size effects induced by the eigen-frequencies of the simulation box.

We have not yet discussed how does the distribution of sound waves varies at each computational cell. In principle, at equilibrium the distribution should be isotropic and density and velocity at any cell should have a similar spectra. In Fig. 6 we show contour plots of the PSD at each cell location, $S_\rho(x,\omega)$. In order to facilitate their reading, the frequency $\omega = 2\pi f$ has been expressed in wavelength units $\lambda = c/f$ and both, position and wavelength, are given in units of the mesh size Δx (i.e. $\lambda/\Delta x$ in abscissas and $x_i/\Delta x$ in ordinates). In the case of NRBC, the position-dependent PSD $S_\rho(x,\omega)$ is almost everywhere flat for all wavelengths larger than the cut-off $\lambda_{cut} \simeq 4\Delta x$ (as stated,

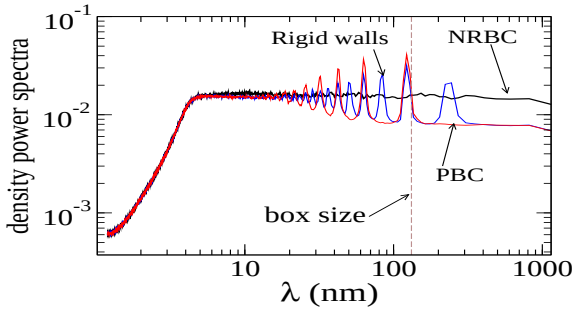

FIG. 5: The spatially averaged power spectral density $\bar{S}_\rho(\omega)$ for argon at $\rho = 1.0\text{gr/cm}^3$ and $T = 300\text{K}$. The simulation domain is $L_x = 135\text{nm}$ and $\Delta x = 1.377\text{nm}$. Comparison between non-reflecting boundaries (NRBC), periodic boundaries (PBC) and rigid walls is made. Frequency $\omega = 2\pi f$ is expressed in wavelength units, $(\lambda = c/f)$, using the sound velocity $c = 577.7\text{m/s}$.

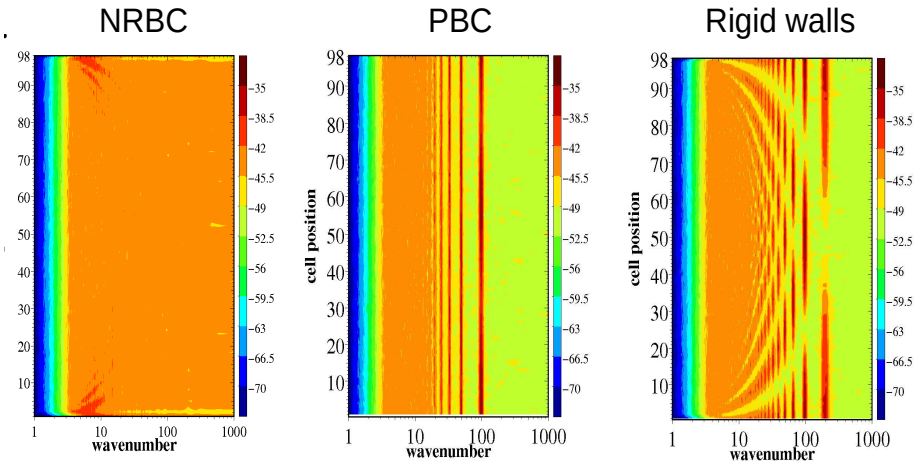

FIG. 6: Contour plot of the PSD of density at each cell of the domain $S_\rho(x_i, \omega)$ for the same cases in Fig. 5: non-reflecting boundaries (NRBC), periodic boundaries (PBC) and rigid walls (RW). The wavelength (abscissas) and the cell position (ordinates) are both given in mesh units Δx. In this units, the box size is $L_x/\Delta x = 98$. We note that in the NRBC case, the spectra remains flat even at $\lambda >> L_x$.

λ_{cut} corresponds to the limiting wavelength resolved by the mesh). It is worthwhile to mention that the NRBC ensures that the spectra remain flat even for frequencies much larger than the box length (in Fig. 6 we are plotting up to $\lambda > 10L_x$). This nice behavior contrasts with what obtained in periodic and purely reflecting (rigid) walls shown in Fig. 6.

As shown in Fig. 6 the spectra obtained with NRBC presents, however, two small regions near the open boundaries where an excess of short wavelentgh is observed. The formation of these "boundary layers" are due to the partial reflection of short waves. Indeed, a closer inspection of Fig. 6 shows that the structure of the local maxima of $S_\rho(x, \lambda)$ at these boundary layers is similar to that produced by purely reflecting rigid walls over the whole spectral range (the reflected waves produce an "echo" whose amplitude has local maxima at $nx_n = m\lambda_m$; n and m being integers.). The main effect of these reflected waves is to increase the local standard deviation (STD) of density $\sigma_\rho(x)$ (or velocity $\sigma_u(x)$) near the open boundary, as can be seen in Fig. 7a. The standard deviation $\sigma_\rho(x)$ decays exponentially towards its equilibrium value at the bulk σ_ρ^{eq} and thus enables to obtain a characteristic length δ, which is a measure (lower bound) of the thickness of the "reflecting boundary layer" (see caption of Fig. 7a). Values of δ calculated for quite different cases are plotted in Fig. 7b. Interestingly, δ scales with the group $(c/\nu_L)\Delta x^2$ which is a measure of the sound absorption length. A wave with wavenumber λ is damped by viscosity at a rate $(2\pi^2)\nu_L/\lambda^2$ (the sound absorption coefficient is $\nu_L/2$). Thus, before being damped, reflected waves are able to penetrate back into the domain up to a distance $\delta_\lambda \simeq c\lambda^2/(2\pi^2\nu_L)$. Inspection of Fig. 6 (for NRBC) indicates that these reflected waves are shorter than a certain wavelenght $\lambda < \lambda_r$ and that they are responsible for the boundary layer thickness; so one expects $\delta \sim \delta_{\lambda_r}$. The trend shown in Fig. 7b indicates $\delta \sim \Delta x^2(c/\nu_L)$, so one concludes that the reflected wavelenghts $\lambda < \lambda_r$ should

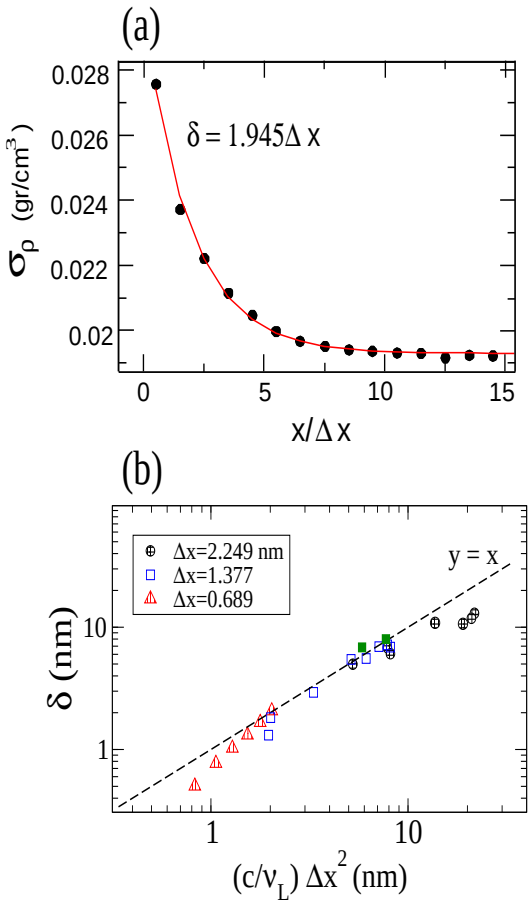

FIG. 7: (a) The standard deviation of the density σ_ρ versus the distance from the open boundary x, for argon at $\rho_{eq} = 1$ gr/cm^3, $T = 300$ and $\Delta x = 0.689$ nm. The value of δ, measuring the thickness of the reflecting boundary layer, is measured using the fit $\sigma_\rho(x) = \sigma_\rho^{eq} + A\exp[-x/\delta]$ (solid line) where σ_ρ^{eq} is the equilibrium value and A is a fitting constant. (b) Values of δ against the sound absorption length $(c/\nu_L)\Delta x^2$. The dashed line indicates the order of magnitude estimate $\delta \sim (c/\nu_L)\Delta x^2$. Results were obtained for a system with $L_x = 134.98$nm, cell volume $V_c = 34.4$nm^3 and different grid spacing Δx. All results for argon at different densities $\rho = [0.17 - 1.34]$ gr/cm^3 and temperatures ($T = 300$K, 178.5K and 476K).

Fluid	ρ (gr/cm^3)	T (K)	c (m/s)	ν_L (cm^2/s)	Δx (nm)	$L/\Delta x$	V_T (nm^3)	$\sigma_{\rho_T}^{(num)}$	$\sigma_{\rho_T}^{(theor)}$ (gr/cm^3)
Water	1.049	300	1467.1	0.4560	2.24944	60	2064.3	0.000939	0.000988
Argon	1.012	476	746.16	0.00158	1.37734	98	3371.8	0.002007	0.001889
Argon	1.012	300	577.72	0.00106	1.37734	98	3371.8	0.001956	0.001923
Argon	1.012	178.5	379.38	0.00132	1.37734	98	3371.8	0.002192	0.002226
Argon	1.349	300	942.15	0.00189	1.37734	98	3371.8	0.001501	0.001366
Argon	1.349	300	942.15	0.00189	0.6885	196	6737.8	0.000875	0.000964

TABLE I: Results obtained for water and argon at different thermodynamic states, longitudinal kinematic viscosities ν_L and several mesh sizes Δx. Comparison is made between the numerical and theoretical standard deviation of the mean density $\sigma_{\bar{\rho}}$. In all cases we used $\delta_R = 0.4$. V_T is the total volume of the system and $L = 397$nm is the system's size in x-direction

only depend on the spatial resolution: this first order estimate yields, $\lambda_r \sim \sqrt{2}\pi\Delta x$. Calculations of the reflection coefficient in Sec. V C confirm this conclusion.

It is interesting to note that, in water, the thickness of the reflecting layer is quite small due to the large viscosity of water ($\eta_L = 4.78$ cP), which yields $(c/\nu_L)_{water} = 0.4\text{nm}^{-1}$. For instance, for $\Delta x = 2.5$nm, the reflecting layer remains restricted to the outermost cell. By constrast, in argon at a similar density $(c/\nu_L)_{argon} = 3.85\text{nm}^{-1}$ so the reflecting layer is visible (as in Fig. 6 and Fig. 7a).

V. RESULTS

A. Equilibrium

Several tests at equilibrium are first required when presenting a fluctuating hydrodynamics solver. Figure 8 shows the standard deviation of the density at one fluid cell, obtained for argon, ranging from gas to liquid. Deviations from the thermodynamic prescription (solid line) are negligible small. Figure 9 shows the standard deviation of the velocity σ_v and density σ_ρ at each fluid cell. Results correspond to the water model. The standard deviation of the velocity is in good agreement with the thermodynamic value $\sqrt{k_B T/(\rho_e V_c)}$, where T is the "input" temperature, V_c the cell's volume and ρ_e the equilibrium density. Deviations are less than few percent (see caption of Fig. 9) and the effective ("output") temperature, $T_o = \rho_e V_c \sigma_v^2/k_B$, deviates about 2 and 6K from the imposed value $T = 300$K in calculations using $\Delta x = 1.37$nm and 2.25nm, respectively.

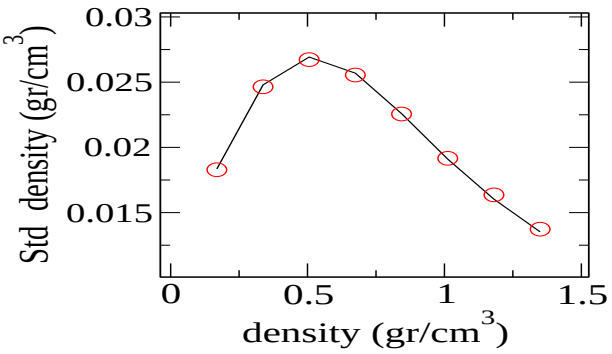

FIG. 8: Standard deviation of the density at one grid cell located in the center computational domain with volume $V_c = 34.4\text{nm}^3$ versus the mean density of the system. Results were obtained for argon equation of state at $T = 300$K, using $L_x = 135$nm and $\Delta x = 0.688$nm. Solid line indicates the prescribed thermodynamic value.

The sudden increase of σ_v near the boundaries observed in Fig. 9(top) is due to the reflection of short waves. As discussed above, in the case of water the width of the reflective boundary layer is quite small (about Δx). The distribution of velocity and density fluctuations is flat along most part of the system and, only the first and second cell adjacent to the boundary deviate from the bulk behavior. As stated before, in the case of argon $\sigma_v(x)$ and $\sigma_\rho(x)$ converges exponentially to the thermodynamic value at the bulk (see Fig. 7a). The STD at the boundaries are typically about 1.4 times larger than within the bulk.

B. Periodic forcing

Another set of tests for the open boundary conditions comprise forcing of sound waves inside the channel. We shall first compare the results obtained using NRBC and periodic boundaries and then calculate the reflection coefficient in our NRBC formulation.

Forcing of waves inside the channel can be done in several ways. For instance, if the objective is to introduce harmonic waves from the *west* boundary (i.e. waves moving right-wise), one can add a sinusoidal term into the A_5 amplitude equation (10):

$$L_5^{(f)} = L_5 + a_{L_5} \cos(\omega_f t) \tag{31}$$

where $L_5^{(f)}$ is the modified L_5, a_{L_5} is proportional to the amplitude of the forced incoming waves and ω_f the forcing (angular) frequency.

Alternatively, it is also possible to add a sinusoidal force (or some mass production term) to the momentum (or density) equation at some cell in the bulk. Both procedures provide similar results; the following tests were done by adding an oscillatory mass source production term in the continuity equation at $x = x_f$,

$$\frac{\partial \rho(x_f, t)}{\partial t} = -\frac{\partial \rho u}{\partial x} + a_\rho \sin(\omega_f t) \tag{32}$$

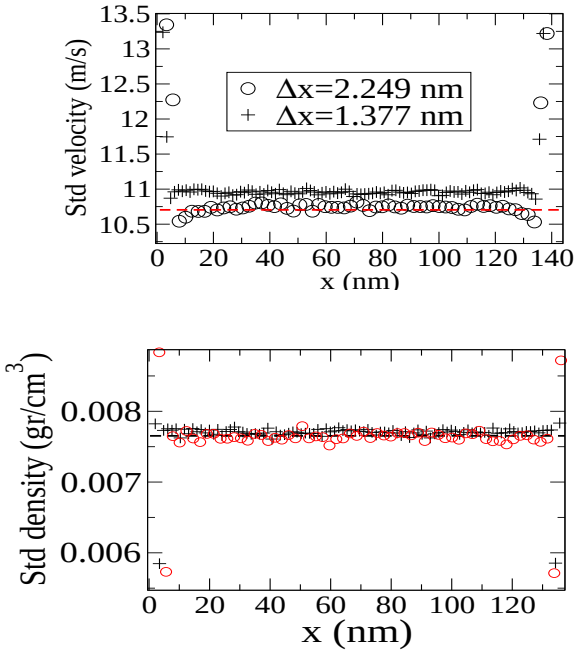

FIG. 9: The standard deviation of velocity (top) and density (bottom) versus the cell position in an equilibrium calculation using the water model. Dashed lines shows the thermodynamic value at the prescribed temperature $T = 300$K. In the case of velocity fluctuations, deviations from respect the thermodynamic value are less than 1% for $\Delta x = 2.249$nm and about 2.3% for $\Delta x = 1.377$nm. Density fluctuations are in very good agreement with the theoretical value.

The latter procedure is useful to study the reflection of short waves because they are damped at such a high rate that their amplitude becomes smaller than thermal noise at relatively short distances from their source. To ensure a significant signal to noise ratio in the study of reflection, we placed the wave source x_f at a distance $x_f = \lambda_f + 5\Delta x$, where λ_f is the wavelength of the forced wave.

Figure 10 compares the spatially dependent power-spectra (as a function of the wavelength, $S_\rho(x, \lambda)$) obtained when forcing waves inside the channel at a certain frequency $w_f = 2\pi c/\lambda_f$ and using either NRBC or PBC. The difference is clear, while in the NRBC case a well defined peak with similar amplitude at every cell of the system is obtained at the forcing frequency ω_f in the PBC case, one gets a complicated x-dependent pattern at the forcing frequency. This pattern is essentially determined by a standing wave which interferes with the eigen-waves of the simulation box at frequencies $\omega_n = 2\pi nc/L$.

C. Reflection coefficient

Figure 11 shows the reflection coefficient obtained using the forcing procedure described above. The reflection coefficient is obtained from the ratio $r = \hat{A}_1/\hat{A}_5$ between the amplitude of the outgoing (imposed) wave $\hat{A}_5$ and the incoming wave $\hat{A}_1$ (resulting from any partial reflection). The amplitude of the waves was calculated from the magnitude of the maximum peak in their Fourier spectra, measured at some cells near the boundary, i.e., $\hat{A}_i = S^{(\max)}_{A_i}(x_b)$, where the "test" position x_b is placed between the open boundary and the forcing cell x_f.

Values of the reflection coefficient are shown in Fig. 11. We note that the values of r obtained from deterministic hydrodynamics (i.e., switching off fluctuations) were found to be similar to those obtained from the fluctuating case. In fact, results for r reported by Polifke *et al.* [29] for large eddy simulations of turbulent flow (also included in Fig. 11a) are consistent with our laminar flow calculations indicating that the behaviour of r with f does not greatly depends on fluctuations, flow or fluid conditions, but rather on the numerical resolution used. In particular, as shown in Fig. 11a, waves with short enought wavelength are partially reflected: we find that irrespective of the fluid properties or flow (fluctuations) conditions, $r \simeq 0.5$ for $\lambda < \lambda_r$ with $\lambda_r \sim 10\Delta x$. This threshold for partial reflection agrees with the estimation done in Sec. IV A and it can be clearly seen in the NRBC case of Fig. 6. Larger wavelengths present a rapid decrease of their reflection coefficient. Our results fit with the trend $r \sim 10^{-3}(f\Delta x)^{1.5}$, shown in dashed line in Fig. 11b. However, the behaviour of r at low frequencies obtained by Polifke *et al.* for turbulent flow scales with

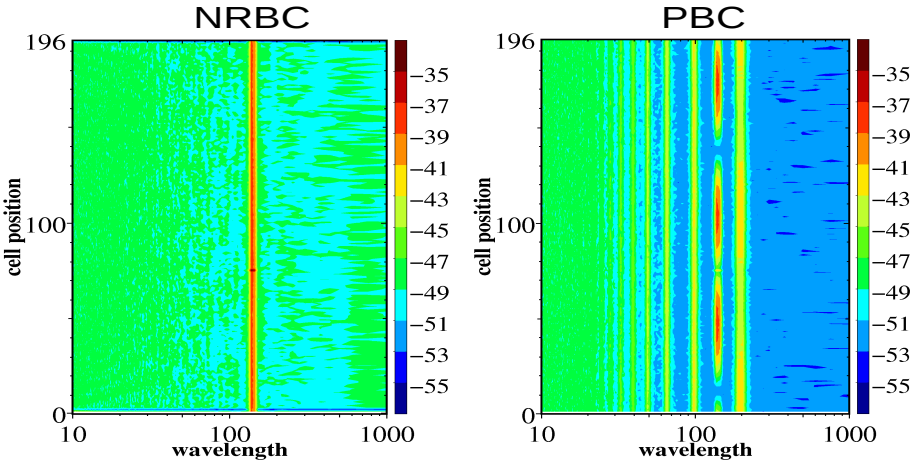

FIG. 10: Contour plot showing the power spectral density (PSD) of the density (in dB) at each cell, under an sinusoidal forcing with wavelength $\lambda_f = 496.32$ nm ($\lambda_f/\Delta x = 135$), induced at cell #75. Wavelength λ and cell positions are given in units of $\Delta x = 0.688$nm. The sound frequency (in Hz) is $f = c/\lambda$, where $c = 942.16$ m/s is the sound velocity. Results were obtained for argon at $\rho = 1.34$gr/cm^3 and $T = 300$K. Comparison is made between non-reflecting boundaries (NRB) and periodic boundary conditions (PBC).

a smaller slope $r \sim f^{0.95}$, suggesting that the type of flow might have some effect on r at low frequencies. We note that the energy of the reflected wave decreases like r^2 so values of $r \sim 0.1$ can be already sought as non-reflecting. In this sense, the trend $r \simeq 10^{-3}(f\Delta x)^{1.5}$ is useful to estimate the spatial resolution (Δx) ensuring evacuation of a given frequency: $f\Delta x \simeq 20$ m/s for $r \simeq 0.1$.

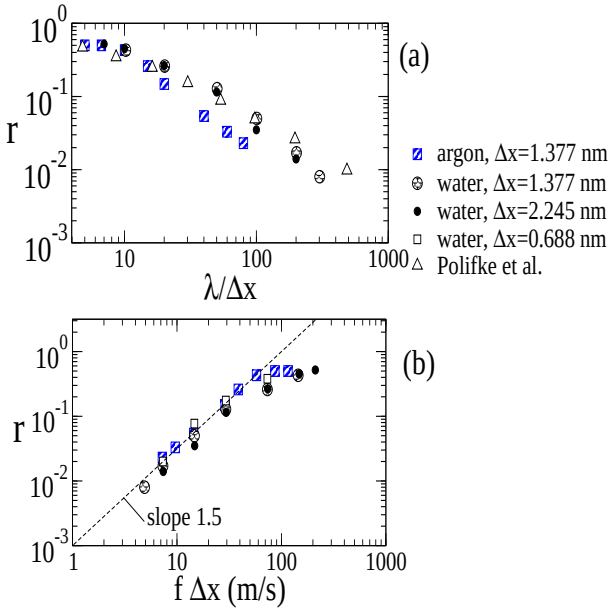

FIG. 11: The reflecion coefficient r calculated as the ratio between maximum amplitudes of the reflected and forced wave $r = \hat{A}_1^{\max}/\hat{A}_5^{\max}$. Results correspond to liquid argon at $\rho = 1.0$gr/cm^3 and water (both at $T = 300$K), whose sound velocities are $c_{argon} = 577.7$m/s and $c_{water} = 1480$ m/s. Results obtained by Polikfke *et al.* [29] from large eddy simulation of turbulent flow have also been included. (a) The reflection coefficient versus the non-dimensional wavelength $\lambda/\Delta x$ and (b) versus the group $f\Delta x$, where $f = \lambda/c$ is the frequency in Hz. The dashed line corresponds to the best fit to our results $r \simeq 10^{-3}(f\,\Delta x)^{1.5}$.

VI. CONCLUSIONS

We have presented a formalism for non-reflecting boundary conditions (NRBC) which allows to evacuate sound waves out of an open fluid domain described by fluctuating hydrodynamics. This set of open boundary conditions, originally derived for standard CFD, consists on solving the linearized Navier-Stokes equations at the open boundary, in the normal-to-boundary direction. A key difference, when dealing with fluctuating hydrodynamics, is the fact that we are considering very small volumes of fluid where mass fluctuations are significant. Therefore, the NRBC formalism should enable the exchange of mass between the computational domain and its surroundings, arising from longitudinal stress fluctuations. These fluctuations are reflected in the variance of the total mass and momentum of the system whose values at equilibrium are prescribed by the grand canonical ensemble thermodynamics. Thus, the purpose of the NRBC in fluctuating hydrodynamics is two fold: first, to evacuate large amplitude sound waves and second, to drive the system to the proper thermodynamical equilibrium. These two requirements are met by a stochastic equation for the amplitude of the incoming waves, which needs to be postulated in the NRBC formalism. On one hand, the deterministic part of this boundary equation ensures the so-called "plane-wave masking" [29] which avoids the reflection of sound waves with amplitudes larger than the thermal noise. On the other hand, the random stress near the boundary acts as a source of random waves into the system. By including the longitudinal stress fluctuations into the boundary equation analysis, we could derive a fluctuation-dissipation balance for the incoming waves amplitude which takes into account the thermodynamic equilibrium conditions to fit the only free parameter of the system: the relaxation rate of the incoming waves, K. We obtained, $K = \nu_L/(\delta_r \Delta x)^2$, where ν_L is the longitudinal kinematic viscosity of the fluid, Δx the computational cell size and δ_R a non-dimensional length. We show that $\delta_R = 0.4$ provides the correct total mass variance regardless of the fluid properties and mesh resolution. An interesting outcome is that the relaxation rate K actually controls the power spectra of density and momentum inside the entire system; this might be useful to tune the sound power spectra in other type of scenarios, such as turbulence.

The present method avoids some of the finite size effects induced by periodic boundaries in fluid-particle simulations and more importantly it provides an useful tool for the simulation of problems involving the propagation of sound waves, such as the design of ultrasound devices or the study of nanoparticle-ultrasound interaction.

VII. ACKNOWLEDGMENTS

Both authors benefit from the Ministerio de Educación y Ciencia "Ramon y Cajal" research contract, funded by the Spanish government. R.D-B acknowledges funding from the Project No. FIS2007-65869-C03-01.

ADD UNED Y EUROPE !!!

APPENDIX A: FLUCTUATING HYDRODYNAMICS IN A STAGGERED GRID

The finite volume method is used to solve the fluctuating Navier-Stokes equations. Spatial gradients are discretized using centered differences and time integration is done by a fully explicit Euler scheme (time step was set to $\Delta t \simeq 10$fs (Courant number $c\Delta t/\Delta x \sim 0.01$). The Euler scheme requires relatively small time steps to keep thermodynamic consistency for density fluctuations. As shown in Ref. [31] more elaborate time integration schemes enable to increase Δt in a factor 10.) Most of the previous works on fluctuating hydrodynamics [17] have implemented their numerical scheme in a collocated grid, whereby all the set of flow variables are resolved at the same position of each volume cell: its center. In this work we have implemented a staggered grid for fluctuating hydrodynamics. The staggered arrangement is illustrated on Fig. 12. Each scalar variable (density and pressure in our case) is computed at the cell centers while the velocity components are resolved at the cell faces. A previous work by Garcia *et al.* [32] made use of a staggered grid-arrangement wherein velocity and temperature were resolved at the integration cell faces and density at the integration cell centers in the aim to well-define the boundary condition on the mass flux.

Compared to a collocated grid, the staggered grid used here provides a much better coupling between the pressure and velocity field. This results in several advantages: first, it avoids the formation of numerical pressure and velocity oscillations (see Patankar [33]) and second, the boundary conditions are well defined. In the staggered arrangement one requires explicit boundary condition for the velocity and density but there is no need of defining an extra boundary condition for the pressure.

We briefly describe the discrete operators involved in a finite volume formulation applied to a staggered grid arrangement, details can be found in Ref. [33]. Conservation equations can be casted in the general form

$$\frac{\partial \rho \Phi}{\partial t} = -\nabla \left(\rho \mathbf{u} \Phi - J_\Phi \right) \tag{A1}$$

where $\Phi = 1$ for mass and $\Phi = \mathbf{u}$ for momentum conservation equations. In the mass equation $\mathbf{J}_1 = 0$ while $\mathbf{J_u} = (p\mathbf{1} + \mathbf{\Pi})$ is the pressure tensor appearing in the momentum equation. The conservation equations (A1) are integrated over control cells of volume V. By integrating (A1) and applying the Gauss theorem to the convection and gradient terms, one gets

$$V\frac{(\rho_c\Phi_c)^k - (\rho_c\Phi_c)^{k-1}}{\Delta t} = -\sum_f \left(\rho_f \mathbf{u_f}\cdot\mathbf{S}_f\Phi_f - [\mathbf{J}_\Phi]_f\cdot\mathbf{S}_f\right)^{k-1}. \tag{A2}$$

The cell center of the integration volume in the above equations is noted by the subscript c, while f stands for the face of the integration domain. Superscript "k" in Eq.(A2) refers to the integration time $t_k = k\Delta t$ and the face area (normal) vector is $\mathbf{S}_f$.

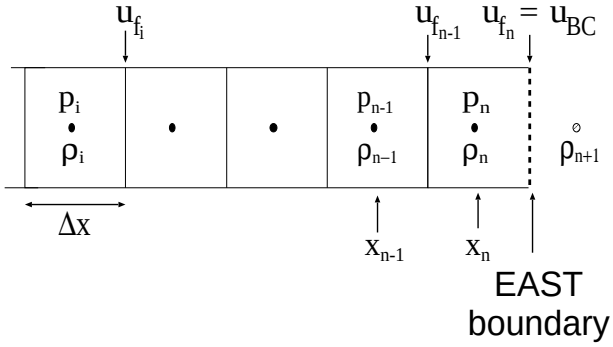

FIG. 12: Staggered grid scheme near the *east* boundary.

As stated, in the staggered grid arrangement the scalar variables (density and pressure) are resolved at the volume cell *center* while the velocity vector components are defined at the cell *faces*, see Fig. 12. To be consistent with this choice, as shown in Fig. 12, the centers of the control cells for the mass equation are placed at the volume cell centers, i.e. $c \to x_i$ in Eq. (A2). In the momentum equation the center of the integration volume is located at the cell faces; i.e. $c \to x_i + \Delta x/2$ in Eq. (A2). As an example, in one dimension, mass equation is integrated over $x_i - \Delta x/2 \le x \le x_i + \Delta x/2$, while momentum equation is integrated over $x_i \le x \le x_{i+1}$. Whenever necessary, variables are interpolated, for instance, the computation in the mass equation of the flux at the face located at $x_i + \Delta x/2$, is calculated as $\rho_f u_f = 0.5(\rho_i + \rho_{i+1})u_f$.

APPENDIX B: NON-REFLECTING BOUNDARY CONDITIONS

For completeness we first describe the implementation of periodic boundaries and rigid walls. At the *west* boundary, *periodic boundary conditions* imply $\rho_0 = \rho_n$ and $u_{f_0} = u_{f_n}$ while at the *east* boundary, $\rho_{n+1} = \rho_1$ and $u_{n+1} = u_1$. *rigid wall boundary conditions* are implemented as $\rho_0 = \rho_1$ and $u_{f_0} = 0$ at the *west* boundary and $\rho_{n+1} = \rho_n$ and $u_{f_n} = 0$ at the *east* boundary. A benefit of the staggered grid arrangement is that boundary conditions on the pressure are not required.

Let us now focus on the implementation of the *non-reflecting boundaries*. We first deal with the *east* outflow boundary. The relations giving the time variation amplitude L_5 [see Eq. (11)] is discretized at the first face cell located upward of the outflow boundary i.e at $x_{n-1} + \Delta x/2$ (see Fig. 12). So that the discretized relations take the form

$$L_5 = \lambda_5\left(\frac{p_n - p_{n-1}}{\Delta x} + \rho_e c\frac{u_n - u_{n-1}}{\Delta x}\right), \quad \lambda_5 = u_{f_{n-1}} + c \tag{B1}$$

where ρ_n, ρ_{n-1}, p_n, p_{n-1}, u_n and u_{n-1} are the values taken at the cell centers located at x_n and x_{n-1}, for the density, pressure and velocity, respectively. Due to the staggered grid arrangement, the velocities u_n and u_{n-1} have to be interpolated, this is done by a simple linear interpolation.

$$u_n = \frac{1}{2}(u_{BC} + u_{f_{n-1}}) \quad \text{and} \quad u_{n-1} = \frac{1}{2}(u_{f_{n-1}} + u_{f_{n-2}}) \tag{B2}$$

The time amplitude variation, L_1 (see Eq. (20)), is also computed at the first face, upwards the outflow boundary condition, so that

$$L_1 = K\rho_e c A_1 \tag{B3}$$

where

$$A_1 = \frac{1}{2}\left(\frac{p_{f_{n-1}} - p_e}{\rho_e c} - u_{f_{n-1}}\right) \tag{B4}$$

where $p_{f_{n-1}}$ is the pressure interpolated at the face cell $n-1$ given by $p_{f_{n-1}} = (p_n + p_{n-1})/2$.

The velocity at the border u_{BC} is solved from numerical integration of Eq. (14), using an Euler scheme,

$$u_{BC}^{t+\Delta t} = u_{BC}^{t} - \frac{\Delta t}{2\rho_e c}\left(L_5^t + L_1^t\right) \tag{B5}$$

The density at the boundary ρ_{BC} could be in principle obtained from time integration of Eq.(15). However, we found that the solution of Eq.(15) leads to numerical instability. Instead, we used an equivalent formulation of the LODI equations based on the spatial gradient at the border (see Ref. [24]),

$$\left(\frac{\partial \rho}{\partial x}\right)_{BC} = \frac{1}{2c^2}\left(\frac{L_5}{\lambda_5} - \frac{L_1}{\lambda_1}\right) \tag{B6}$$

where λ_1 is given in Eq. (B9).

By defining ρ_{n+1} as the density at the ghost cell $n+1$ (required to define ρ_{BC} and $(\partial\rho/\partial x)_{BC}$), the density value at the *east* frontier of the domain is given as following

$$\rho_{n+1} = \rho_n + \left(\frac{\partial \rho}{\partial x}\right)_{BC} \Delta x \tag{B7}$$

At equilibrium and low Reynolds number calculations considered here, the density gradient at the boundary was found to be negligible small. In practice, the zero mass flux condition,

$$\rho_{n+1} = \rho_n \quad (\rho_{BC} = \rho_n) \tag{B8}$$

was found to provide similar results to Eq. (B7).

For the derivation of the open boundary condition at the *west* border of the computational domain, one needs to note that the outgoing waves now correspond to the amplitudes A_5 and incoming wave to A_1. Also, one needs to take into account that the $x-$axis is reversed. The variation of the outgoing wave is thus computed from

$$L_1 = -\lambda_1\left(\frac{p_2 - p_1}{\Delta x} - \rho_e c \frac{u_2 - u_1}{\Delta x}\right), \quad \lambda_1 = u_{f_1} - c \tag{B9}$$

while the incoming wave variation is approximated by

$$L_5 = -K\rho_e c A_5 \tag{B10}$$

with

$$A_5 = \frac{1}{2}\left(\frac{p_{f_1} - p_e}{\rho_e c} + u_{f_1}\right) \tag{B11}$$

u_1, u_2 and p_{f_1} are estimated by linear interpolation.

---

[1] L. D. Landau and E. M. Lifshitz. *Fluid Mechanics*. Pergamon Press, New York, 1959.

[2] J. Keizer. *Statistical Thermodynamics of Non-Equilibrium Processes*. Springer-Verlag, New York, 1987.

[3] T. Colonius. Modeling artificial boundary conditions for compressible flow. *Annual Review of Fluid Mechanics*, 36:315–345, 2004.

[4] J. Christensen, A. I. Fernandez-Dominguez, F. Leon-Perez, L. Martin-Moreno, and F. J. Garcia-Vidal. Collimation of sound assisted by acoustic surface waves. *Nature Physics*, 3(12):851–852, 2007.
[5] A. Haake and J. Dual. Contactless micromanipulation of small particles by an ultrasound field excited by a vibrating body. *J. Acoust. Soc. Am.*, 117:2752–2760, 2005.
[6] J. A. Cosgrove, J.M. Buick, D. M. Campbella, and C. A. Greated. Numerical simulation of particle motion in an ultrasound field using the lattice Boltzmann model. *Ultrasonics*, 43:21–25, 2004.
[7] O. Berk Usta, Anthony J. C. Ladd, and Jason E. Butler. Lattice Boltzmann simulations of the dynamics of polymer solutions in periodic and confined geometries. *J. Chem. Phys.*, 122:094902, 2005.
[8] G. Giupponi, G. De Fabritiis, and P.V. Coveney. An hybrid model for the simulation of macromolecular dynamics. *J. Chem. Phys*, 126:154903, 2007.
[9] R. Adhikari, K. Stratford, M. E. Cates, and A. J. Wagner. Fluctuating lattice Boltzmann. *Europhys. Lett.*, 71:473–479, 2005.
[10] G. De Fabritiis, R. Delgado-Buscalioni, and P. Coveney. Modelling the mesoscale with molecular specificity. *Phys. Rev. Lett*, 97:134501, 2006.
[11] S. Williams, J.B. Bell, and A. L. Garcia. Algorithm refinement for fluctuating hydrodynamics. *SIAM Multiscale Modeling and Simulation*, 6:1256–1280, 2008.
[12] M. Serrano and P. Español. Thermodynamically consistent mesoscopic fluid particle model. *Phys. Rev. E*, 64:046115, 2001.
[13] R. Delgado-Buscalioni and G. De Fabritiis. Embedding molecular dynamics within fluctuating hydrodynamics in multiscale simulations of liquids. *Phys. Rev. E*, 76:036709, 2007.
[14] R. Delgado-Buscalioni. Cyclic dynamics of a tethered polymer under shear flow. *Phys. Rev. Lett.*, 96:088303, 2006.
[15] A. Donev, A. L. Garcia, and B.J. Alder. An event-driven hybrid molecular dynamics and direct simulation Monte Carlo algorithm. *J. Comp. Phys.*, 227:2644–2665, 2008.
[16] R. Delgado-Buscalioni, P.V. Coveney, and G. De Fabritiis. Towards multiscale modelling of complex liquids using hybrid particle-continuum schemes. *Journal of Mechanical Engineering Science, Proceedings of the Institution of Mechanical Engineers, Part C*, page in press, 2008.
[17] G. De Fabritiis, M. Serrano, R. Delgado-Buscalioni, and P. V. Coveney. Fluctuating hydrodynamic modelling of fluids at the nanoscale. *Phys. Rev. E.*, 75:026307, 2007.
[18] K. Johnson, J. A. Zollweg, and K. E. Gubbins. The Lennard-Jones equation of state revisited. *Mol. Phys.*, 78:591, 1993.
[19] D. M. Heyes. Shear viscosity of Lennard-Jones fluid. *Chem. Phys. Lett.*, 153:319, 1988.
[20] T.J. Poinsot and S.K. Lele. Boundary conditions for direct simulations of compressible viscous flows. *Journal of Computational Physics*, 101:104–129, 1991.
[21] G. W. Hedstrom. Non reflective boundary conditions for nonlinear hyperbolic systems. *Journal of Computational Physics*, 30:222–37, 1979.
[22] K. W. Thompson. Time dependent boundary conditions for hyperbolic systems. *Journal of Computational Physics*, 68:1–24, 1987.
[23] Jean Pierre Boon and Sidney Yip. *Molecular Hydrodynamics*. Dover Pubns., 1992.
[24] T. Poinsot and D. Veynante. *Theoretical and Numerical Combustion*. 2nd Ed., Edwards, 2005.
[25] J. C. Strikwerda. Initial boundary value problem for incompletely parabolic systems. *Commun. Pure Appl. Math.*, 30:797, 1977.
[26] J. Oliger and A. Sundstrom. Theoretical and practical aspects of some initial boundary value problems in fluid dynamics. *SIAM J. Appl. Math*, 35:419–446, 1978.
[27] D. H. Rudy and J. C. Strikwerda. A non-reflecting outflow boundary condition for subsonic Navier-Stokes calculations. *Journal of Computational Physics*, 36:55–70, 1980.
[28] L. Selle, F.Nicoud, and T. Poinsot. The actual impedance of non-reflecting boundary conditions: implications for the computation of resonators. *AIAA Journal*, 42:958–964, 2004.
[29] W. Polifke and P. Moin C. Wall. Partially reflecting and non-reflecting boundary conditions for simulation of compressible viscous flow. *Journal of Computational Physics*, 213:437–449, 2006.
[30] N. C. Nigam. *Introduction to Random Vibrations (Structural Mechanics)*. MIT Press, Boston, USA, 1983.
[31] J.B. Bell, A. L. Garcia, and S. Williams. Numerical methods for the stochastic Landau-Lifshitz Navier-Stokes equations. *Phys. Rev. E*, 76:016708, 2007.
[32] A. L. Garcia, M. M. Mansour, G. C. Lie and E. Clementi. Numerical integration of the fluctuating hydrodynamic equations. *Journal of Statistical Physics*, 47-2:209–228, 1987.
[33] S.V. Patankar. *Numerical Heat Transfer and Fluid Flow*. Hemisphere publishing corporation, McGraw-Hill book company, 1991.
[34] By making use Eq. 18, it is possible to calculate the reflection coefficient $R(\omega) = A_1/A_5$ [29], which takes the form $r(\omega) = K/(K^2 + 4\omega^2)^{(1/2)}$, where ω is the wave angular-frequency.
[35] For arbitrary γ one has $A_1 = (1/2)(\delta p/(\rho_e c_S) - \delta u)$, $\langle \delta p^2 \rangle = c_T^2 c_S^2 \langle \delta \rho^2 \rangle$ and $\langle \delta \rho^2 \rangle = \rho_e k_B T/(c_T^2 V_c)$, where c_T and c_S are the isothermal and adiabatic sound velocities ($c_S^2 = \gamma c_T^2$). These relations lead to the same result of Eq. (27).
[36] For instance, in the evaluation of L_i [see Eq. (11)], pressure and velocity gradients arising from outgoing waves should be measured *at* the boundary; however, numerically, this is not possible and these gradients are in practice evaluated at a small distance from the open boundary (in our implementation, one cell away Δx from it).
[37] We guess that depending on the details of the numerical implementation of the open boundaries, one might obtain a slightly different optimum value of δ_R.